Applied Catalysis B: Environmental 307 (2022) 121136

Contents lists available at ScienceDirect

Applied Catalysis B: Environmental

journal homepage: www.elsevier.com/locate/apcatb

Nanoflower-branch LDHs and CoNi alloy derived from electrospun carbon nanofibers for efficient oxygen electrocatalysis in microbial fuel cells

Huiyu Li [a,b,c], Yaxin Sun [a,b,c], Jiaona Wang [d], Yuanfeng Liu [a,b,c], Congju Li [a,b,c,*]

[a] Energy Conservation and Environmental Protection Engineering Research Center in Universities of Beijing, Beijing 100083, China
[b] Beijing Key Laboratory of Resource-oriented Treatment of Industrial pollutants, Beijing 100083, China
[c] School of Energy and Environmental Engineering, University of Science and Technology Beijing, Beijing 100083, China
[d] School of Materials Science & Engineering, Beijing Institute of Fashion Technology, Beijing Key Laboratory of Clothing Materials R & D and Assessment, Beijing 100029, China

ARTICLE INFO

Keywords:
Microbial fuel cells
Oxygen reduction reaction
Layered double hydroxides
Carbon nanofiber
CoNi alloy

ABSTRACT

Designing rational nanostructure to promote the oxygen reduction reaction (ORR) catalytic activity of microbial fuel cells (MFCs) is desirable but still remains a huge challenge. In this work, an elaborately designed strategy is proposed to deposit layered double hydroxides (LDHs) on the surface of ZIF-67 grown along nanofibers, thereby obtaining nanoflower-branch composites (CoNi-LDH@CNFs) with a rich cavity structure supported by electrospinning nanofibers. During the pyrolysis process, the variable cobalt in ZIFs is captured by LDHs nanosheets to generate CoNi alloy. As expected, CoNi-LDH@CNFs exhibits brilliant ORR catalytic activity. The as-prepared catalyst is an outstanding cathode in MFC, with a maximum power density of 1390.37 mW/m^2, superior to Pt/C corresponding MFC (843.67 mW/m^2). Impressively, the nanofiber-derived catalyst exhibits long-term durability in single-chamber MFCs. This work provides a new perspective for the combination of LDHs and nanofiber-derived materials, and gives promising performance in realistic MFCs applications.

1. Introduction

As the main necessary energy, fossil energy poses a great threat to human health and climate change. Environmental problems and energy reserves are still the most pressing issues hindering sustainable development [1–4]. Microbial fuel cells (MFCs) can convert chemical energy in organic compounds into obtainable electrical energy through biocatalytic reactions under anaerobic conditions [5,6]. MFCs hold great potential to simultaneously meet with the two major challenges of energy crisis and environmental pollution. However, after microorganisms transfer electrons from the anode to the cathode, the oxygen reduction reaction (ORR) rate of the cathode is slower than that of the anode, which easily causes electron accumulation [7,8]. Therefore, one of the major challenges facing MFCs applications is the cathode catalyst, as its ability to regulate the ORR rate and eventually affecting the overall performance [9]. The commercially available Pt/C catalysts increases the cost and reduces the ORR efficiency with corrosion and biological contamination [10]. To avert that, it is highly desirable to develop alternative non-noble metal catalysts to improve ORR activity, such as biocatalysts, transition metal oxides, carbon-based materials and their composites [11,12]. The advances of these ORR catalysts can even be comparable to Pt/C, demonstrating the great potential of non-precious metal materials in the development of excellent performance and low-cost MFCs catalysts.

Up to now, layered double hydroxides (LDHs), known as anionic clays, have been emerging as one of the most well studied layered materials [13–16]. LDHs are composed of brucite-like layers, in which part of the divalent metal cations are coordinated by hydroxyl octahedrons, which can form a positively charged layer after being isomorphically substituted by trivalent metal cations [17,18]. As a type of inorganic lamellar material, LDHs containing two or more transition metals are exploited into single-layer nanosheets, which maximize the effectiveness of each single layer. In particular, the positively charged LDHs surface is suitable for oxygen adsorption and concomitant ORR, which is expected to exhibit reasonable catalytic performance in fuel cells [19]. Unfortunately, traditional preparation methods such as co-precipitation, ion exchange, and hydrothermal methods reduce the performance of two-dimensional (2D) LDHs materials, as induced poor conductivity, low active site exposure and bonding between OOH*/OH* intermediates and metal active sites [20,21]. To address these technical

* Corresponding author at: Energy Conservation and Environmental Protection Engineering Research Center in Universities of Beijing, Beijing 100083, China.
E-mail address: congjuli@126.com (C. Li).

https://doi.org/10.1016/j.apcatb.2022.121136
Received 1 November 2021; Received in revised form 18 January 2022; Accepted 21 January 2022
Available online 24 January 2022

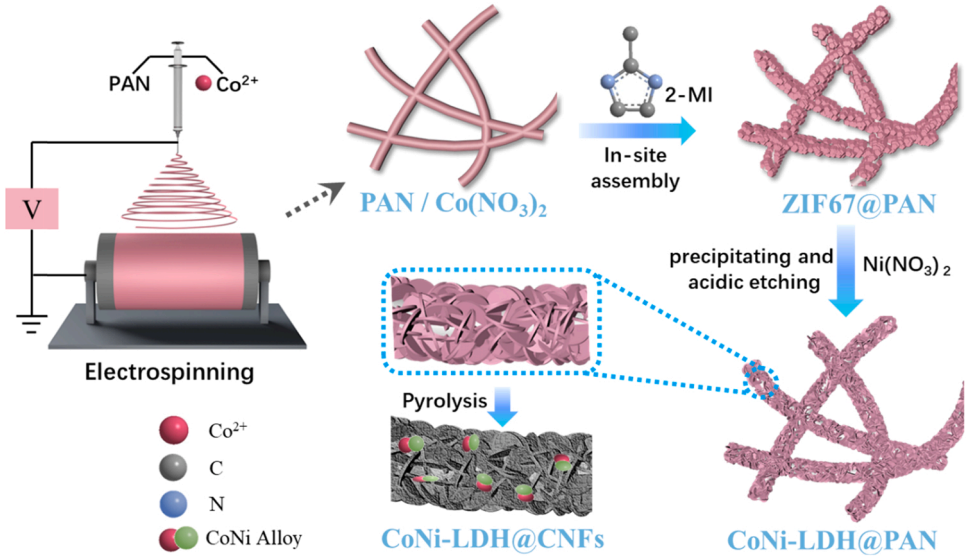

Fig. 1. Schematic illustration of the synthesis of CoNi-LDH@CNFs.

issues, recent studies have confirmed that three-dimensional (3D) metal-based hydroxides and their composites doped with multiple heteroatoms (such as N, B, S, P or F) can become a class of promising bifunctional catalysts [22–24]. The existence of multi-electron orbitals, favorable electronic structure and remarkable metal-like characteristics show more abundant Faraday redox reactions, higher conductivity and stability.

To provide a more convenient electron transmission path and avoid LDHs powder agglomeration and clog, significant research efforts have been devoted and successfully anchored LDHs on membranes or shape-bodies to get high current density [17,25,26]. Specifically, Duan et al. immobilized LDHs on Ni foam, conducting cloth and fluorine-doped tin oxide (FTO) to demonstrate high oxygen reduction performance [27]. Tang et al. successfully introduced LDHs into the graphene framework as an electrocatalyst through electrochemical synthesis. As it is known, polyacrylonitrile (PAN) nanofibers prepared by electrospinning technology have a simple preparation method, high porosity and good conductivity after carbonization, and can be used as supporting substrates to achieve orderly accumulation of 2D catalytic materials [28]. Nevertheless, there are rarely reports that electrospun nanofibers can be used as conductive carbon substrates to realize satisfactory ordered stacking of LDHs.

Inspired by this, LDHs were successfully evenly decorated on the surface of nanofibers, and CoNi-LDH@PAN nanofibers were designed by electrospinning technology. As an excellent template, PAN can be converted into conductive carbon fiber with stable structure after carbonization at high temperature. A deformable LDHs material was etched and deposited on the surface of the synthetic ZIF-67 frame, creating a rich cavity structure to enhance the performance. The overall fabrication process of composite is schematically illustrated in Fig. 1. By adjusting the pH of the nitrate precursor of LDHs, a uniform nanoflower-branch structure was obtained. In addition to the elegant design, the variable cobalt in ZIFs can provide trivalent ions for LDHs material, and form CoNi alloy with Ni in nanoflowers in the subsequent process, which is also crucial for controlling the electrocatalytic activity of ORR. As such, the strong synergistic effect between the nanoflower-branch structure and the active components of the alloy endowed the prepared material with excellent ORR catalytic activity, resulting in high power density and coulombic efficiency in the cathode application of MFCs. Moreover, the catalyst exhibited long-term durability, showing broad prospect in single-chamber MFCs cathode.

2. Materials and methods

2.1. In-situ assembly ZIF67@PAN

0.6 g Co $(NO_3)_2.6H_2O$ was stirred and ultrasonic dispersed in 6 mL N, N-dimethylformamide (DMF, 99.5%). Then 0.6 g Polyacrylonitrile (PAN, M_w = 150,000) and 0.15 g Poly(vinylpyrrolidone) (PVP, $M_w = 1.3 \times 10^6$) were added under ultrasound and stirred continuously for 24 h. The evenly stirred viscous solution was then poured into a 10 mL plastic syringe and connected to a high-voltage supply. At room temperature, the electrostatic spinning process was carried out at a distance of 20 cm between the aluminum foil collector and the tip. The syringe pump controlled the feed rate at 0.8 mL / h, and the high voltage and low voltage were 16 kV and − 1 kV, respectively. 0.1 g obtained precursor fiber was immersed in 15 mL methanol solution containing 0.1 g 2-methylimidazole (2-MI), soaked at room temperature for 6 h, washed with ethanol twice to obtain ZIF67@PAN.

2.2. Preparation of CoNi-LDH@PAN

0.1 g of ZIF67-PAN was dispersed into 20 mL ethanol solution containing 30 mg, 60 mg and 120 mg Ni $(NO_3)_2.6H_2O$ (5 mM, 10 mM and 20 mM), respectively. Then the reaction vessel was placed in an ultrasonic bath at room temperature for 1 h. Finally, the products were washed with ethanol once and dried overnight at 60 ℃ to obtain CoNi-LDH@PAN with different Ni $(NO_3)_2.6H_2O$ concentrations. The obtained samples were named CoNi-LDH@PAN-5 mM, CoNi-LDH@PAN-10 mM and CoNi-LDH@PAN-20 mM.

2.3. Preparation of CoNi-LDH@CNFs

The as prepared ZIF67@PAN and CoNi-LDH@PAN were further annealed from room temperature to 350°, maintained for 20 min, then raised to 800° at 5°/min, maintained for 2 h, and then naturally cooled down. The obtained samples were named Co@CNFs, CoNi-LDH@CNFs-5 mM, CoNi-LDH@CNFs-10 mM, CoNi-LDH@CNFs-20 mM.

2.4. Materials characterization

The microscopic morphology was observed by scanning electron microscopy (SEM, NOVANANOSEM450). Lattice fringes and selected area electron diffraction pattern were measured by transmission electron microscopy (TEM) and high resolution transmission electron

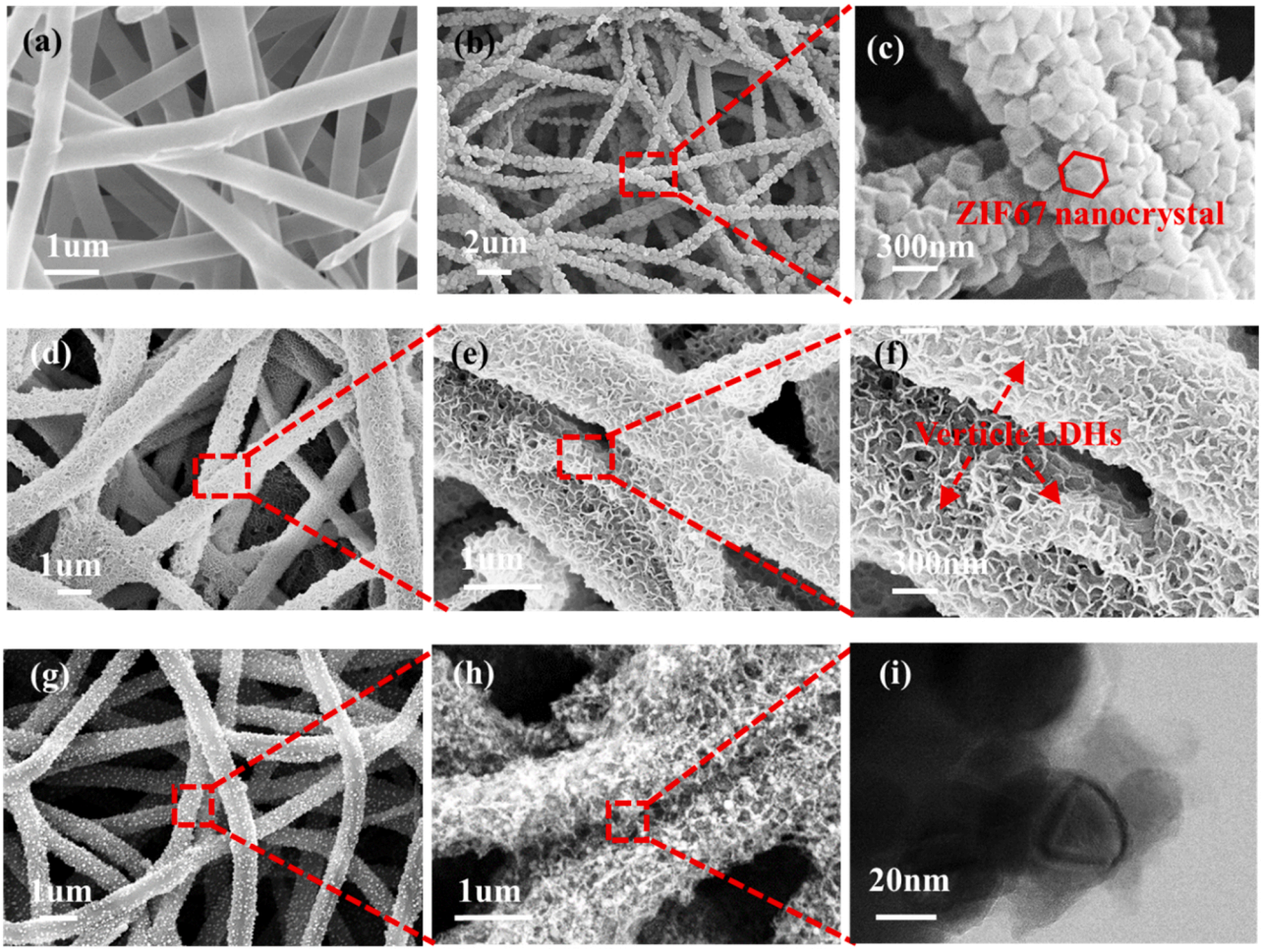

Fig. 2. SEM images of (a) CNFs, (b-c) ZIF67@PAN, (d-f) CoNi-LDH@PAN-10 mM, (g-h) CoNi-LDH@CNFs-10 mM, (i) TEM image of CoNi-LDH@CNFs-10 mM.

microscopy (HRTEM) at 200 kV using JEM-2200fs. X-ray diffraction (XRD) data was collected by Bruker TTR3 diffractometer with copper Kα radiation (λ = 1.5418). Nitrogen adsorption-desorption curves were measured at 77 K utilizing the Brunauer-Emmett-Teller (BET) method (ASAP-2460). The surface chemical composition was investigated by X-ray photoelectron spectroscopy (XPS, PHI5000 VersaprobeIII).

2.5. Electrochemical measurements

Firstly, 1 mg of the prepared catalyst was mixed with 750 μL isopropanol and 250 μL Nafion solution (DuPont, 5%), then coated on stainless steel (SS) and let dry naturally to obtain a working electrode (1 cm * 1 cm). All electrochemical data were collected by electrochemical analysis station (CHI760E, CH Instrument Company, Shanghai, China) using a three-electrode system. The Pt sheet and the saturated calomel electrode (SCE) were served as the counter electrode and reference electrode, respectively. PBS buffer solution (0.62 g/L NH_4Cl, 5.54 g/L $NaH_2PO_4.2\,H_2O$, 23.08 g/L $Na_2HPO_4.12\,H_2O$ and 0.26 g/L KCl) was used as the electrolyte. The cyclic voltammetry (CV) was operated at − 0.8–0.4 V (vs. SCE) with a scan rate of 10 mV/s. The linear sweep voltammetry (LSV) was carried out from − 0.8 to 0.4 V (vs. SCE) and the scan rate was 10 mV/s. The electrochemical impedance spectroscopy (EIS) was performed under the open circuit potential (OCP) with a frequency of 10^5-0.1 Hz. The Tafel curve was conducted in the overpotential range of 0–0.1 V with a scan rate of 1 mV/s.

2.6. MFCs construction and operation

This study was based on the single-chamber MFCs, using carbon cloth (WOS1009, Taiwan CeTech Co. Ltd, China) as the bioanode (7 cm^2) and cathode diffusion layer (8 cm * 8 cm), while the prepared composites and the control Pt/C (JM 20% Pt/C, HISPEC 4000) were used as the cathode catalytic layer (3.5 cm * 3.5 cm). The prepared catalyst and Nafion solution were evenly mixed in isopropyl alcohol (mass ratio 1:4:2), and the resulting paste was repeatedly coated on cathode diffusion layer to dry. PBS buffer solution, trace minerals (10 mL/L) and vitamins (1 mL/L) were mixed with activated sludge. 2 g/L sodium acetate was used as the electron donor. The external resistance of 1000 Ω was connected between cathode and anode. When the OCP remained stable, the MFCs was ready for electrochemical analysis.

3. Results and discussion

3.1. Material characterization

The morphology and structure of the composite material were evidenced by scanning electron microscopy (SEM). Fig. 2(a) showed a nanofiber precursor containing Co^{2+} seeds obtained by electrospinning technology. As shown in Fig. 2(b-c), the micro-nano morphology of ZIF67-PAN confirmed that Co-based MOFs with polyhedral structure were successfully grown on the surface of PAN nanofibers by in-situ growth method. The fibers coated by dense and uniform MOFs were connected to each other and formed a 3D layered structure with large

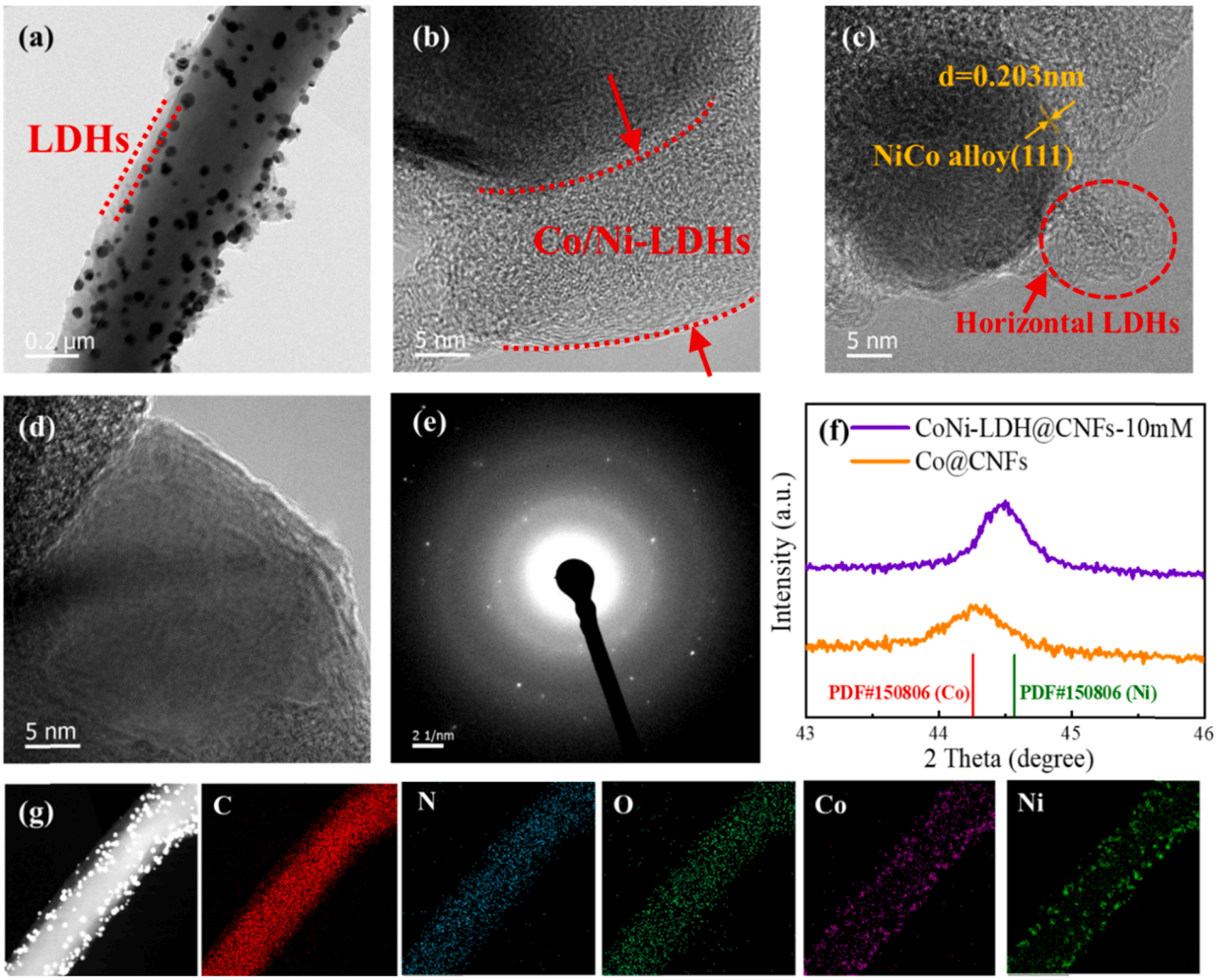

Fig. 3. (a-d) TEM images, (e) Selected area electron diffraction (SAED) pattern, (f) Partially magnified XRD patterns corresponding to the main peak of CoNi alloy, (g) TEM image and corresponding element mappings of CoNi-LDH@CNFs-10 mM.

pores, providing a 3D template for the subsequent uniform co-precipitation of LDHs with controllable morphology [29]. Subsequently, after the addition of nickel nitrate, a layer of nanoflower-like LDHs was obviously formed on the surface of ZIF-67 in Fig. 2(d)-(f). This is because in the ultrasonic process, the Ni ions hydrolyzed to produce the proton H^+, which can chemically etch the ZIF-67 framework. As protons were consumed, the amount of hydroxide ions in the solution increased. Meanwhile, Co ions released from ZIF-67 were partially oxidized by O_2 and NO^{3-}. Then, Co^{2+}/Co^{3+} ions co-precipitated with Ni ions to form a layer of LDHs around ZIF-67 [30]. Interestingly, the load of LDHs on nanofibers can be adjusted by the concentration of nitrate. This may be due to the different hydrolysis rate of nitrate at different concentrations, which lead to changes in the number of nucleation sites of LDHs [31]. CoNi-LDH@PAN-5 mM (Fig. S1(a)) had low hydrolysis rate, resulting in fewer nucleation sites and sparse nanosheets. Correspondingly, 20 mM nitrate (Fig. S1(c)) produced the largest number of nanosheets with deposition and agglomeration. After high temperature annealing, Fig. 2(g)-(h) still maintained a complete carbon nanofiber structure, which can be used as a carrier to more effectively prevent the corrosion of CoNi alloy in solution [32]. In addition, an abundance of nanoflower-like structures was observed on the surface of carbon nanofibers, although the cobalt-nickel-catalyzed nanosheets caused shrinkage and entanglement. Large-scale cracks were considered to be a rich microporous and mesoporous structure, which can provide sufficient contact area between the electrocatalyst and the electrolyte [33].

The TEM observation further revealed the details of the morphology and nanostructure of the catalysts. As shown in Fig. 3(a)-(b), a layer of 10–20 nm nanosheet can be clearly observed on the surface of PAN fibers. These ultra-thin nanosheets can produce a large number of medium pores and a high specific surface area, which shorten the electron/ion transfer path and provide a convenient channel for mass diffusion [34]. Moreover, many particle-like projections were scattered around the nanosheets. The magnified nanoparticles were clearly presented in Fig. 3(c-d), where the observed clear lattice spacing with a lattice distance of 0.203 nm between adjacent layers were corresponded to the (111) crystallographic plane of the CoNi alloy [35]. It is consistent with the peak corresponding to CoNi alloy detected in the XRD patterns. The partially magnified XRD patterns corresponding to the main peak of CoNi alloy with reference to Fig. 3(f). Fig. 3(g) further confirmed the element distribution and composition of the CoNi-LDH@CNFs, that is, O, C and N were evenly distributed in the entire area of carbon nanofibers and LDHs in the catalyst, while Ni and Co only appear on the LDHs and nanoparticles. Notably, consistent with the SEM results, only corrosion and deposition occurred on the outer surface of ZIF after adding nickel nitrate, resulting in the formation of LDHs.

In order to further investigate the crystal structure of the catalysts, the results of the XRD patterns were displayed in Fig. 4(a). The three characteristic peaks were located at 44.4°, 51.7° and 76.0°, which were exactly between the peaks of Co (JCPDS 15–0806) and Ni (JCPDS

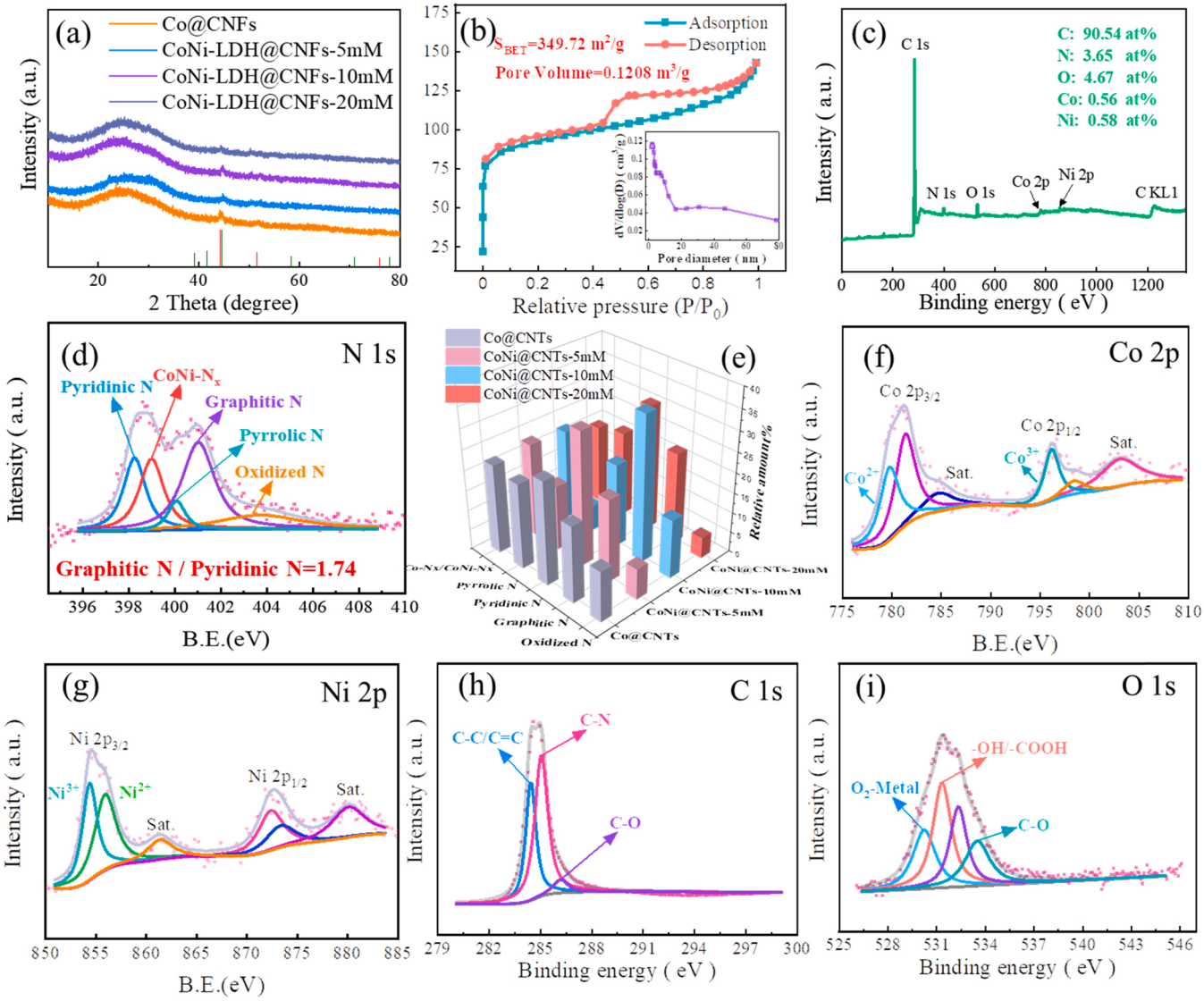

Fig. 4. (a) XRD patterns corresponding to as-prepared catalysts. (b) N_2 adsorption–desorption isotherm curve of CoNi-LDH@CNFs-10 mM (inset: the corresponding pore size distribution curve). XPS spectrum of CoNi-LDH@CNFs-10 mM: (c) survey spectrum, (d) N 1s, (e) The content of different N type from XPS result, (f) Co 2p, (g) Ni 2p, (h) C 1s and (i) O 1s.

04–0850), and matched the crystal planes of CoNi alloy (111), (200) and (220), respectively [36]. It is consistent with the lattice spacing observed by TEM, which further proved the existence of CoNi alloy. The relatively broad peak at 26.1° was attributed to the (002) crystal plane of graphitic carbon. This is due to the shrinkage of the CoNi alloy lattice, indicating that the CoNi alloy nanoparticles successfully induced and catalyzed NCNFs [37].

N_2 adsorption-desorption and pore measurement were used to clarify the pore structure and size distribution of the catalysts. The BET specific surface area (SSAs) and BJH pore size distribution diagrams were illustrated in Fig. 4(b). The N_2 adsorption-desorption curves showed typical type IV isotherm characteristics, indicating that the catalysts had abundant mesoporous and macroporous structures [38]. Compared with Co @CNFs in Fig. S4(b) (269.49 m^2/g), the SSAs of CoNi-LDH@CNFs-10 mM increased significantly after adding LDHs nanoflower structure (349.72 m^2/g). This result was consistent with a sharp rise in isotherms at high relative pressure as shown in Fig. 4(b) [39]. It is worth noting that the pore size distribution curve of CoNi-LDH@CNFs-10 mM in inset of Fig. 4(b) showed a multi-level pore distribution, confirming the internal micropores (peak pores are about ca. 0–2 nm) and mesopores (peak pores are about ca. 2–40 nm) coexist. Mainly benefiting from the introduction of LDHs, the larger SSAs and increased pores gave a favorable contact environment for the electrolyte, thereby promoting the more smooth diffusion of the reactants to the active sites. Meanwhile, it is beneficial to expose more active sites and maintaining the overall efficiency of the catalytic process.

The chemical composition and electronic structure of the catalysts were further investigated by X-ray photoelectron spectroscopy (XPS). The presence of C, N, O, Co and Ni was confirmed by XPS survey spectrum in Fig. 4(c), which was consistent with TEM mapping results. Table S1 listed the specific element content of several composite materials in XPS spectrum, among which the content of C was always higher than other elements. Moreover, it could be deduced that N was successfully doped into the nanofiber composites as the isoatomic active sites, and the combination of different contents of LDHs and N affected the electrocatalytic activity. In the N 2p spectrum of CoNi-LDH@CNFs-10 mM (Fig. 4(d)), five different nitrogen-type peaks were detected, which were corresponded to pyridinic-N (398.26 eV), pyrrolic-N (400.1 eV), graphitic-N (401.28 eV) and oxidized N (403.9 eV), respectively. Notably, after adding LDHs, CoNi-N_x active substance in the CoNi-LDH@CNFs can be detected at 399.12 eV [40]. It has been extensively investigated that graphite nitrogen (N combined with three

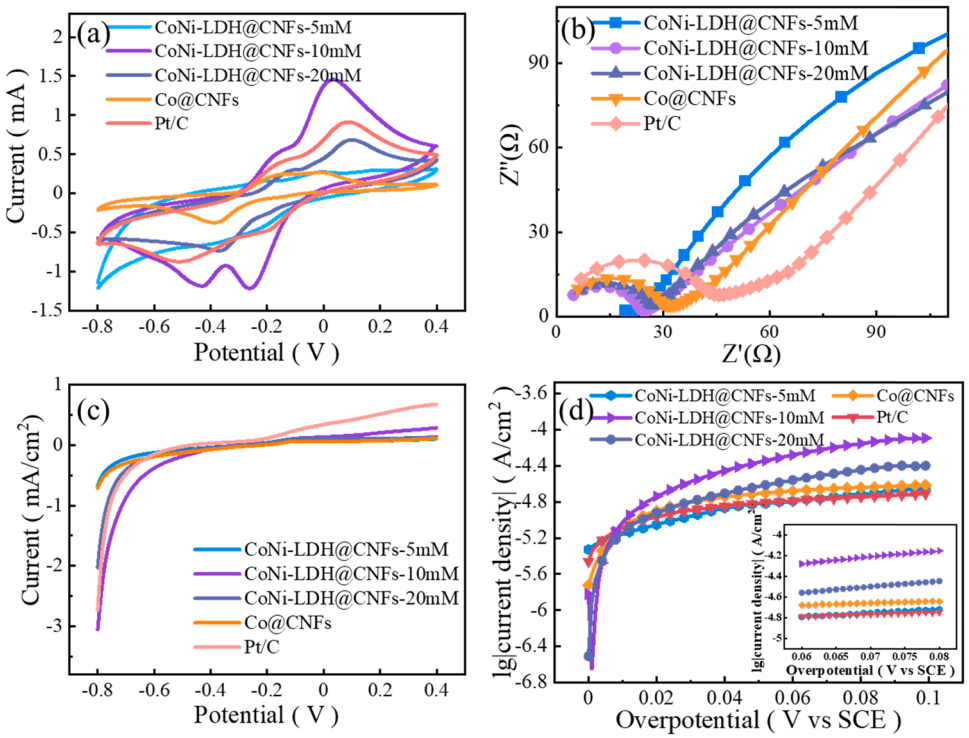

Fig. 5. Comparative the as-prepared catalysts (a) CV curves at a scan rate of 10 mv/s in PBS electrolyte, (b) Nyquist plots of EIS, (c) LSV curves at a scan rate of 10 mv/s in PBS electrolyte, (d) Tafel curves at a scan rate of 1 mv/s in PBS electrolyte (inset: the linear fitting results for Tafel curves of overpotential from 60 to 80 mV).

carbon atoms) can promote electron transfer and increase conductivity by affecting the electronic and geometric structure of carbon [41]. In particular, the percentage of graphitic-N/pyridinic-N can be used as a reference to influence the catalytic activity by increasing the electronic conductivity of the material [36]. According to different types of N content in Fig. 4(e) and Table S2, it was found that the content of graphite nitrogen in the CoNi-LDH@CNFs-10 mM was the highest. In this study, the ratio of graphitic-N/pyridinic-N increased from 0.74 to 1.74 after adding appropriate LDHs, which was conducive to the improvement of catalytic activity. The Co 2P spectrum can be split into Co $2P_{1/2}$ (796.0 eV) and Co $2p_{3/2}$ (780.5 eV) in Fig. 4(f). Co $2p_{3/2}$ can be divided into three forms: Co^{2+} (780.41 eV), Co-N_x (782.5 eV) and satellite peak (787 eV) [42], among which the formation of Co-N, a favorable ORR active site, had been confirmed. The co-existence of Co^{2+} and Co^{3+} species was due to the partial oxidation of Co nanoparticles on the surface of LDHs in the form of a thin cobalt oxide layer [28]. Furthermore, the Co 2p orbital in CoNi-LDH@CNFs transferred to a higher binding energy than that in Co@CNFs, indicating electron transfer from the carbon nanofiber surface to CoNi alloy [36]. Fig. 4(g) showed the spectrum of Ni 2P. Ni $2P_{3/2}$ at 855.1 eV can be divided into Ni (853.9 eV) and Ni^{2+} (855.9 eV) metal states. The partial oxidation of Ni^{+} from the outer surface of CoNi alloy catalyzed the change of the electronic structure of Co and Ni. It also indicated the formation of CoNi alloy and the existence of bimetallic synergy, especially CoNi alloy redistributed Co between Ni, thus facilitating the adsorption of reaction intermediates in ORR electrocatalysis [33]. The C 1s spectrum in Fig. 4 (h) included five diffraction peaks centered at 284.6 eV, 285.1 eV and 286.2 eV, which can be attributed to C−C/C═C, C−N and C−O groups [43]. According to the intensity, C 1s spectrum was mainly composed of C−C/C═C and C-N. The high resolution spectrum of O 1s can be split into four peaks (Fig. 4(i)), which were O_2-metal (530.1 eV), oxygen-containing groups (-OH and -COOH) (531.1 eV), surface absorbed water (532.2 eV) and carbon-based oxygen in C-O (533.3 eV), respectively [34,44].

3.2. Electrochemical characterization

The standard three-electrode system revealed the ORR kinetics of the prepared catalysts, and the results were displayed in Fig. 5. The CV curves (Fig. 5(a)) clearly observed the electrode activity of the five catalysts in the redox reaction. Among them, the Co@CNFs catalyst had a weak oxidation peak and an obvious reduction peak, which corresponded to the ORR reaction at the catalytic active sites of Co. Compared with Co@CNFs, the three CoNi-LDH@CNFs with different nitrate concentrations were significantly better in current density. This may correspond to the doping of Ni increased the active center, and the corrosion of nickel nitrate was beneficial to expose the active center and increase the active sites. Furthermore, it was found that the catalyst CoNi-LDH@CNFs with a nickel nitrate concentration of 10 mM had the most obvious redox peak and produced the largest current density, which may profited from the highest graphite nitrogen content in the XPS results. In addition, the ohmic resistance (R_{ohm}) and charge transfer resistance (R_{ct}) are crucial factors for electrochemical reactions. Under the OCP, the electrochemical impedance (EIS) of five catalysts Co@CNFs, CoNi-LDH@CNFs-5 mM, CoNi-LDH@CNFs-10 mM, CoNi-LDH@CNFs-20 mM and Pt/C were further tested, and the results were illustrated in Fig. 5(b). The ohmic resistance values corresponding to the above five catalysts were 19.38, 4.765, 6.785, 6.038 and 6.945, respectively. Meanwhile, the R_{ct} of the three CoNi-LDH@CNFs was significantly smaller than that of the Co@CNFs, which confirmed that the deposition of LDHs corroded the surface of ZIF polyhedra framework into nanosheets, leading to the decrease of R_{ohm} and R_{ct}. Especially CoNi-LDH@CNFs-10 mM was the smallest and even better than that of Pt/C, which meant that the appropriate number of nanosheets were more likely to undergo charge transfer at the electrode/electrolyte interface and had higher electron transfer efficiency.

The as-prepared catalysts were further analyzed as ORR electrocatalysts in 0.1 M PBS electrolyte by using LSV, as depicted in Fig. 5(c). The CoNi-LDH@CNFs-10 mM found in Table S3 had the highest onset

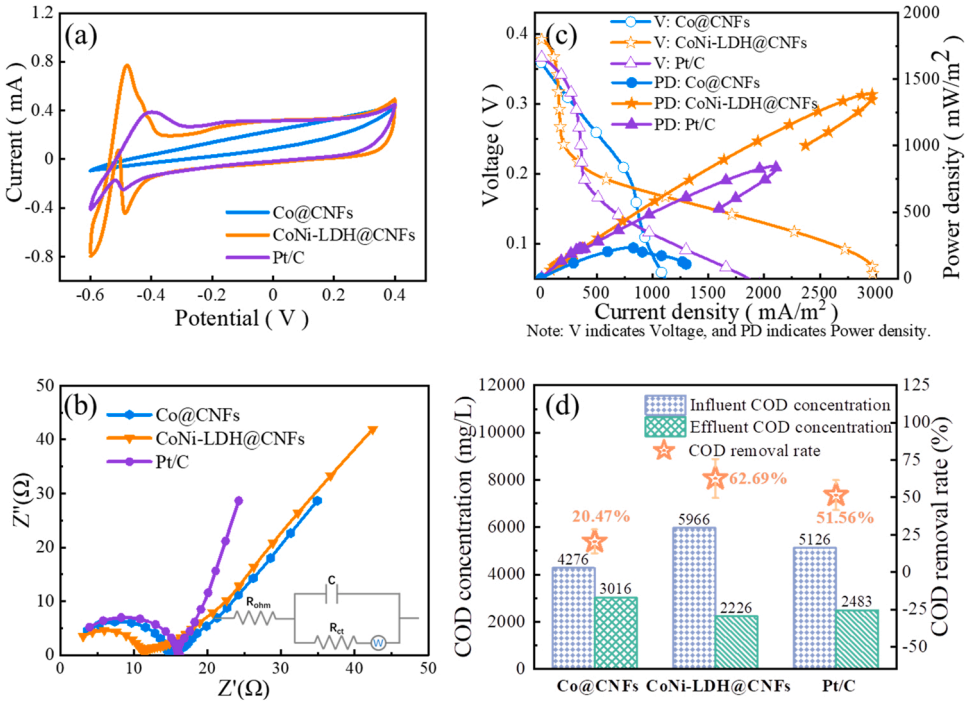

Fig. 6. Comparative MFCs equipped with different cathode catalysts: (a) Cyclic voltammetry curves, (b) Nyquist plots of EIS (inset: equivalent circuit model), (c) Polarization curves, (d) The effect of COD in MFCs influent and effluent and removal rate.

Table 1
Power performance of MFCs modified with different electrocatalysts cathode.

Reactor	Open circuit voltage (V)	PD (mW/m^2)	R_{in}	CE (%)
MFC-Co@CNFs	0.561 ± 0.015	233.56	4.548	21.1
MFC-CoNi-LDH@CNFs	0.641 ± 0.007	1390.37	3.476	15.3
MFC-Pt/C	0.599 ± 0.078	843.67	5.176	11.8

potential (E_0) (−0.222 V) and a higher limit current density (J_D) than Pt /C (3.052 and 2.796 mA / cm^2), which confirmed that the catalyst can take full advantage of bimetallic Co/Ni and ample nanoflower structure in ORR electrocatalytic reaction. Fig. 5(d) showed the Tafel curves of the prepared catalysts. According to the Eq. S1, the fitting calculation results of the Tafel at the equilibrium potential were listed in Table S4. Consistent with the results of EIS and LSV, the corresponding k value of CoNi-LDH@CNFs-10 mM was much larger than that of Pt/C, and the exchange current density (j_0) was almost twice that of Pt/C (0.223 $\times 10^{-4}$ A/cm^2 and 0.123 $\times 10^{-4}$ A/cm^2, respectively). It is stated that the corresponding electrode had the largest electron transfer rate, and can reduce oxygen molecules at a faster reduction rate, thereby obtaining a greater current density, and had the potential for application in MFCs.

3.3. MFCs performances

Since CoNi-LDH@CNFs-10 mM is expected to get higher power output in MFCs applications, the above catalyst, Co@CNFs and commercial 20% Pt/C were simultaneously operated as the cathode catalyst of MFCs, and they were named MFC-CoNi-LDH@CNFs, MFC-Co@CNFs and MFC-Pt/C. After the output voltage of the three MFCs was maintaining stably for three cycles, the influence of different catalysts on the performance of the MFCs was discussed. In order to evaluate the electrode surface activity corresponding to the catalyst, the CV and EIS curves of three MFCs were measured on the electrochemical workstation. In the voltage range of − 0.6–0.4 V (vs. SCE), MFC-CoNi-LDH@CNFs, MFC-Co@CNFs and MFC-Pt/C showed obvious redox peaks (Fig. 6a), suggesting that the catalysts showed excellent ORR catalytic activity in practical application. The R_{ohm} of the three MFCs in Fig. 6(b) was 3.476 Ω, 4.548 Ω and 5.176 Ω respectively, and the R_{ct} of the MFC corresponding to CoNi-LDH@CNFs catalyst was significantly lower than that of the other two MFCs. This trend was consistent with the open circuit voltage in Table 1. Lower R_{ohm} and R_{ct} are conducive to improving the surface conductivity, which in turn improves the ORR electron transport capacity between the "water-flooded" three-phase interface in the MFCs cathode.

Polarization curves and output power were effective method to evaluate MFCs performance. The corresponding results were calculated by referring to Eq. S2 and revealed in Fig. 6(c). Notably, the voltage of the MFC-CoNi-LDH@CNFs decreased more slowly with the increase of the current density, indicating that the electrode surface had better ORR activity and charge transfer rate [45]. Furthermore, the maximum output power of MFC equipped with the catalyst CoNi-LDH@CNFs can reach 1390.37 mW/m^2, which was far greater than that of MFC-Pt/C, 843.67 mW/m^2 (Table 1). On a concluding note, the MFC with CoNi-LDH@CNFs catalyst had high electricity production capacity, which can be attributed to the nanoflower structure on the surface of nanofibers that maximized the exposure of the active sites, thereby increasing its utilization. In addition, this superior structure can also promote the transportation of oxygen molecules and provide more effective surface area in contact with the substrate. Apart from this, CoNi alloy provided ample catalytic sites for ORR, which tended to change the ORR mechanism from 2e$^-$ pathway to 4e$^-$.

Chemical oxygen demand (COD) can be used as a time dependent parameter in MFCs system to evaluate microbial efficiency. Fig. 6(d) declared the average influent and effluent and corresponding COD removal rates of the three MFCs in several operating cycles. As intended, the COD removal rate of MFC-CoNi-LDH@CNFs reached 62.69%, which was higher than the 51.56% of MFC-Pt/C. In fact, the observed COD removal was directly related to the respective MFCs performance, because the increase in ORR led to higher microbial utilization of the substrate, which ultimately led to higher energy output of the system. In addition, the COD removal rate of MFC-Co@CNFs was only 20.47%, which corresponded to its lower voltage output power. This may be due

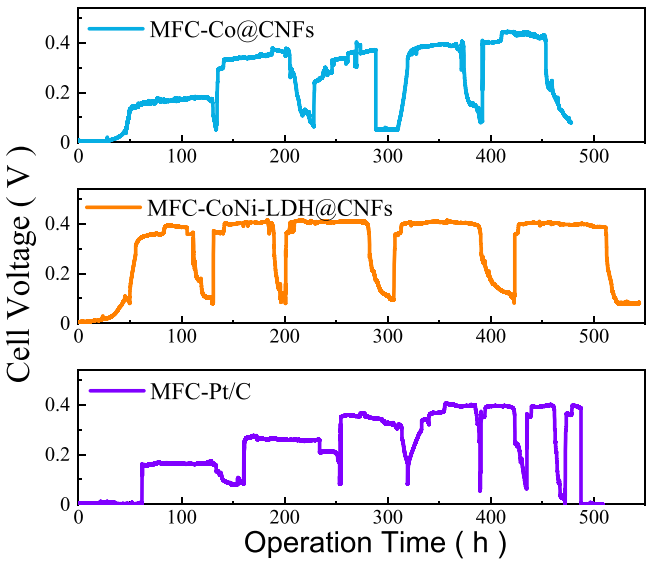

Fig. 7. The output voltage of MFCs supported by prepared electrocatalysts and commercial Pt/C cathodes.

to the slow kinetics of the cathode, causing inadequate and accurate utilization of the electrons at the three-phase interface. Furthermore, the coulombic efficiency (CE) can evaluate the ability of the reactor to convert the chemical energy recovered in the organic matter into electrical energy, which was calculated by Eq. S4. As presented in Table 1, significant differences in the CE of these MFCs were also noted during stable periods. Among them, MFC-Pt/C had the lowest CE, 11.8%. Corresponding to the EIS result, the MFC with low charge transfer internal resistance was easier to transfer electrons to the cathode surface smoothly. The results of CE also indicate that CNFs-derived catalysts have higher and more effective wastewater treatment capabilities in MFCs applications.

To maintain stable activity in the MFCs cathode three-phase interface, the durability of the catalysts needs to be assessed. Initially, the output voltage of all MFCs in Fig. 7(a) showed a rapid increase, and the start-up time of MFC-Pt/C was slightly slower than the other two. This demonstrated that the CNFs-derived catalysts with 3D ordered network structure were conducive to reducing the activation energy barrier of ORR, thereby accelerating the smooth construction of the cathode reaction. Subsequently, it was found that MFC-CoNi-LDH@CNFs exhibited good stability during operation, and the maximum output voltage could almost be maintained at 0.41 V after several cycles. This confirmed that the corresponding catalyst had excellent electrochemical performance and long-term suitability, even better than commercial Pt/C.

4. Conclusion

In summary, the nanoflower structure was grown uniformly on the surface of the electrospun nanofiber by in-situ growth method. The cavity structure was elaborately manufactured by depositing LDHs on the surface of the MOFs. As such, the as-prepared catalyst had a large specific surface area and a multi-level pore distribution. The electrochemical behavior in neutral solution was carefully investigated. It was found that the catalyst can exhibit the most superior electrocatalytic activity when the concentration of LDHs precursor nickel nitrate solution was 10 mM. The maximum output power of MFC equipped with as-prepared catalyst cathode was significantly higher than that of commercial Pt/C, which originated from the CoNi alloy as a vital active site to accelerate the oxygen reduction reaction. The catalyst with nanoflower-branch structure can be a promising candidate for substituting noble metal in MFCs cathode.

CRediT authorship contribution statement

Huiyu Li: Conceptualization, Methodology, Validation, Data analysis, Writing – original draft. **Yaxin Sun:** Data analysis, Writing – review & editing. **Jiaona Wang:** Resources, Writing – review & editing. **Yuanfeng Liu:** Methodology, Validation. **Congju Li:** Conceptualization, Resources, Supervision.

Declaration of Competing Interest

The authors declare that they have no known competing financial interests or personal relationships that could have appeared to influence the work reported in this paper.

Acknowledgements

This work is supported by the National Natural Science Foundation of China (NSFC No. 52170019, 51973015 and 21274006), Beijing Natural Science Foundation (2202029) and the Fundamental Research Funds for the Central Universities (No. 06500100, 06121062 and FRF-TP-19–046AIZ), and the “Ten thousand plan”-National High-level personnel of special support program. National Environmental and Energy Science and Technology International Cooperation Base.

Appendix A. Supporting information

Supplementary data associated with this article can be found in the online version at doi:10.1016/j.apcatb.2022.121136.

References

[1] Y. Liu, X. Zhang, H. Li, et al., Porous α-Fe2O3 nanofiber combined with carbon nanotube as anode to enhance the bioelectricity generation for microbial fuel cell, Electrochim. Acta 391 (2021), 138984.
[2] A. Wang, K. Shi, D. Ning, et al., Electrical selection for planktonic sludge microbial community function and assembly, Water Res. 206 (2021), 117744.
[3] J. Chen, L. Jiang, J. Yang, et al., Enhanced electrochemical performance in microbial fuel cell with carbon nanotube/NiCoAl-layered double hydroxide nanosheets as air-cathode, Int. J. Hydrog. Energy 46 (73) (2021) 36466–36476.
[4] L. Peng, Y. Sun, S. Guo, et al., Highly efficient construction of hollow Co-Nx nanocube cage dispersion implanted with porous carbonized nanofibers for Li-O2 batteries, J. Mater. Chem. A. (2022).
[5] S. Narayanasamy, J. Jayaprakash, Application of carbon-polymer based composite electrodes for microbial fuel cells, Rev. Environ. Sci. Biotechnol. 19 (3) (2020) 595–620.
[6] J.S. Lee, K. Jo, T. Lee, et al., Facile synthesis of hybrid graphene and carbon nanotubes as a metal-free electrocatalyst with active dual interfaces for efficient oxygen reduction reaction, J. Mater. Chem. A 1 (34) (2013) 9603–9607.
[7] D.Y. Chung, J.M. Yoo, Y. Sung, Highly durable and active pt-based nanoscale design for fuel-cell oxygen-reduction electrocatalysts, Adv. Mater. 30 (42) (2018), 1704123.
[8] J. Chen, J. Yang, L. Jiang, et al., Improved electrochemical performances by Ni-catecholate-based metal organic framework grown on NiCoAl-layered double hydroxide/multi-wall carbon nanotubes as cathode catalyst in microbial fuel cells, Bioresour. Technol. 337 (2021), 125430.
[9] P. Pattanayak, N. Pramanik, F. Papiya, et al., Metal-free keratin modified poly (pyrrole-co-aniline)-reduced graphene oxide based nanocomposite materials: a promising cathode catalyst in microbial fuel cell application, J. Environ. Chem. Eng. 8 (3) (2020), 103813.
[10] F. Papiya, P. Pattanayak, P. Kumar, et al., Development of highly efficient bimetallic nanocomposite cathode catalyst, composed of Ni:Co supported sulfonated polyaniline for application in microbial fuel cells, Electrochim. Acta 282 (2018) 931–945.
[11] Q. Li, R. Cao, J. Cho, et al., Nanocarbon electrocatalysts for oxygen reduction in alkaline media for advanced energy conversion and storage, Adv. Energy Mater. 4 (6) (2014), 1301415.
[12] H. Wang, L. Jiang, J. Chen, et al., Enhanced bioelectrochemical performance caused by porous metal-organic framework MIL-53(Fe) as the catalyst in microbial fuel cells, Process Biochem. 99 (2020) 147–153.
[13] J. Yu, Q. Wang, D. O'Hare, et al., Preparation of two dimensional layered double hydroxide nanosheets and their applications, Chem. Soc. Rev. 46 (19) (2017) 595–5974.
[14] G. Fan, F. Li, D. Evans, et al., Catalytic applications of layered double hydroxides: recent advances and perspectives, Chem. Soc. Rev. 45 (50) (2015) 7040–7066.
[15] L. Jiang, J. Chen, D. Han, et al., Potential of core-shell NiFe layered double hydroxide@Co3O4 nanostructures as cathode catalysts for oxygen reduction reaction in microbial fuel cells, J. Power Sources 453 (2020), 227877.

[16] L. Jiang, J. Chen, Y. An, et al., Enhanced electrochemical performance by nickel-iron layered double hydroxides (LDH) coated on Fe3O4 as a cathode catalyst for single-chamber microbial fuel cells, Sci. Total Environ. 745 (2020), 141163.
[17] M.F.P. Duarte, I.M. Rocha, J.L. Figueiredo, et al., CoMn-LDH@carbon nanotube composites: bifunctional electrocatalysts for oxygen reactions, Catal. Today 301 (2018) 17–24.
[18] D. Chen, C. Chen, Z.M. Baiyee, et al., Nonstoichiometric oxides as low-cost and highly-efficient oxygen reduction/evolution catalysts for low-temperature electrochemical devices, Chem. Rev. 115 (18) (2015) 9869–9921.
[19] H. Huang, S. Zhou, C. Yu, et al., Rapid and energy-efficient microwave pyrolysis for high-yield production of highly-active bifunctional electrocatalysts for water splitting, Energy Environ. Sci. 13 (2020).
[20] W. Wang, Y. Liu, J. Li, et al., NiFe LDH nanodots anchored on 3D macro/mesoporous carbon as a high-performance ORR/OER bifunctional electrocatalyst, J. Mater. Chem. A 6 (29) (2018) 14299–14306.
[21] T. Zhan, X. Liu, S. Lu, et al., Nitrogen doped NiFe layered double hydroxide/reduced graphene oxide mesoporous nanosphere as an effective bifunctional electrocatalyst for oxygen reduction and evolution reactions, Appl. Catal. B Environ. 205 (2017) 551–558.
[22] H. Wu, Z. Chen, Y. Wang, et al., Regulating the allocation of N and P in codoped graphene: via supramolecular control to remarkably boost hydrogen evolution, Energy Environ. Sci. 12 (9) (2019) 2697–2705.
[23] J. Quílez-Bermejo, E. Morallón, D. Cazorla-Amorós, Metal-free heteroatom-doped carbon-based catalysts for ORR: a critical assessment about the role of heteroatoms, Carbon 165 (2020) 434–454.
[24] S. Chen, L. Zhao, J. Ma, et al., Edge-doping modulation of N, P-codoped porous carbon spheres for high-performance rechargeable Zn-air batteries, Nano Energy 60 (2019) 536–544.
[25] G. Jia, Y. Hu, Q. Qian, et al., Formation of hierarchical structure composed of (Co/Ni)Mn-LDH nanosheets on MWCNT backbones for efficient electrocatalytic water oxidation, ACS Appl. Mater. Interfaces 8 (23) (2016) 14527–14534.
[26] G. Zhang, J. Xing, Y. Zhao, et al., Hierarchical N,P co-doped graphene aerogels framework assembling vertically grown CoMn-LDH nanosheets as efficient bifunctional electrocatalyst for rechargeable Zinc-air battery, J. Colloid Interface Sci. 590 (2021) 476–486.
[27] Z. Li, M. Shao, H. An, et al., Fast electrosynthesis of Fe-containing layered double hydroxide arrays toward highly efficient electrocatalytic oxidation reactions, Chem. Sci. 6 (11) (2015) 6624–6631.
[28] C. Feng, Y. Guo, Y. Xie, et al., Bamboo-like nitrogen-doped porous carbon nanofibers encapsulated nickel–cobalt alloy nanoparticles composite material derived from the electrospun fiber of a bimetal–organic framework as efficient bifunctional oxygen electrocatalysts, Nanoscale 12 (2020) 5942–5952.
[29] D. Ji, S. Peng, L. Fan, et al., Thin MoS2 nanosheets grafted MOFs-derived porous Co–N–C flakes grown on electrospun carbon nanofibers as self-supported bifunctional catalysts for overall water splitting, J. Mater. Chem. A 5 (45) (2017) 23898–23908.
[30] J. Lai, B. Huang, Y. Chao, et al., Strongly coupled nickel-cobalt nitrides/carbon hybrid nanocages with Pt-like activity for hydrogen evolution catalysis, Adv. Mater. 31 (2) (2019).
[31] Z. Jiang, Z. Li, Z. Qin, et al., LDH nanocages synthesized with MOF templates and their high performance as supercapacitors, Nanoscale 5 (23) (2013) 11770.
[32] S. Surendran, S. Shanmugapriya, A. Sivanantham, et al., Electrospun carbon nanofibers encapsulated with NiCoP: a multifunctional electrode for supercapattery and oxygen reduction, oxygen evolution, and hydrogen evolution reactions, Adv. Energy Mater. 8 (20) (2018), 1800555.
[33] Y. Xie, C. Feng, Y. Guo, et al., MOFs derived carbon nanotubes coated CoNi alloy nanocomposites with N-doped rich-defect and abundant cavity structure as efficient trifunctional electrocatalyst, Appl. Surf. Sci. 536 (2021), 147786.
[34] C. Chen, H. Su, L. Lu, et al., Interfacing spinel NiCo2O4 and NiCo alloy derived N-doped carbon nanotubes for enhanced oxygen electrocatalysis, Chem. Eng. J. 408 (2021), 127814.
[35] L. Zeng, X. Cui, L. Chen, et al., Non-noble bimetallic alloy encased in nitrogen-doped nanotubes as a highly active and durable electrocatalyst for oxygen reduction reaction, Carbon 114 (2017) 347–355.
[36] Y. Fu, H. Yu, C. Jiang, et al., NiCo alloy nanoparticles decorated on n-doped carbon nanofibers as highly active and durable oxygen electrocatalyst, Adv. Funct. Mater. 28 (9) (2018), 1705094.
[37] L. Zeng, X. Cui, L. Chen, et al., Non-noble bimetallic alloy encased in nitrogen-doped nanotubes as a highly active and durable electrocatalyst for oxygen reduction reaction, Carbon (2017).
[38] A Y H, B Z L, B M Z, et al., Amorphous Fe2O3 nanoshells coated on carbonized bacterial cellulose nanofibers as a flexible anode for high-performance lithium ion batteries, J. Power Sources 307 (2016) 649–656.
[39] Y. Zhu, Y. Liu, Y. Liu, et al., Heteroatom-doped hierarchical porous carbons as high-performance metal-free oxygen reduction electrocatalysts, J. Mater. Chem. A. 3 (22) (2015) 11725–11729.
[40] L. Zeng, X. Cui, L. Chen, et al., Non-noble bimetallic alloy encased in nitrogen-doped nanotubes as a highly active and durable electrocatalyst for oxygen reduction reaction, Carbon 114 (2017) 347–355.
[41] B. Liang, Y. Zhao, M. Zong, et al., Hierarchically porous N-doped carbon encapsulating CoO/MgO as superior cathode catalyst for microbial fuel cell, Chem. Eng. J. 385 (2020), 123861.
[42] J. Dai, D. Zhao, W. Sun, et al., Cu(II) ions induced structural transformation of cobalt selenides for remarkable enhancement in oxygen/hydrogen electrocatalysis, ACS Catal. 9 (12) (2019) 10761–10772.
[43] P. Liu, S. Gao, Y. Wang, et al., Core–shell CoNi@graphitic carbon decorated on B,N-codoped hollow carbon polyhedrons toward lightweight and high-efficiency microwave attenuation, ACS Appl. Mater. Interfaces 11 (28) (2019) 25624–25635.
[44] S. Wei, T. Chen, Q. Wang, et al., Metal-organic framework derived hollow CoFe@C composites by the tunable chemical composition for efficient microwave absorption, J. Colloid Interface Sci. 593 (2021) 370–379.
[45] H. Li, X. Zhang, Y. Qin, et al., Crafting controllable Fe-based hierarchically organic-frameworks from bacterial cellulose nanofibers for efficient electrocatalysts in microbial fuel cells, J. Power Sources 512 (2021), 230522.